Available online at www.sciencedirect.com
ScienceDirect
International Journal of Heat and Fluid Flow 28 (2007) 127–144
International Journal of HEAT AND FLUID FLOW
www.elsevier.com/locate/ijhff

Interface–turbulence interactions in large-scale bubbling processes

Petar Liovic, Djamel Lakehal *

Institute of Energy Technology, ETH Zurich, and ASCOMP GmbH, Technoparkstrasse 1, CH-8005 Zurich, Switzerland

Received 9 February 2005; received in revised form 11 November 2005; accepted 10 March 2006
Available online 22 May 2006

Abstract

A novel large-eddy simulation (LES) approach for computation of incompressible multi-fluid flows is presented and applied to a turbulent bubbling process driven by the downward injection of air into a water pool at $Re_{pipe} \approx 17{,}000$. Turbulence is found to assume its highest intensity in the bulk of the gas flow, and to decay as the interface of the growing bubble is approached. Shear flow prevails in the area of jetting from the pipe, buoyancy-driven flow prevails away from the jetting region, and a third region of vigorous bubble break-up lay $O(10^0)$–$O(10^1)$ pipe diameters above the tip. Cascading of turbulent kinetic energy is accompanied by an instability-induced linear cascading of interface length scales (i.e. azimuthal modes), transferring energy from the most unstable mode to the smallest interface deformation scales. The LES shows the out-scatter of energy from the large-scale gas-side vortices down to interface wrinkling scales, and statistics prove the existence of a strong correlation between turbulence and interface deformations. Surface curvature was found to constitute a source of small-scale vorticity, and therefore of dissipation of turbulent kinetic energy.

Keywords: Large-eddy simulation; Bubbling; Interface wrinkling; VOF

1. Introduction

Bubbling mechanisms and induced mixing occur in a large range of multi-phase flow systems, with a significant sub-set of these processes featuring large bubble injection to sustain the flow. Driven by high-volume, moderate velocity gas injection into liquid baths, such flows are often chaotic and turbulent, and can feature a wide spectrum of interfacial length scales. The turbulence resulting from large bubble injection alters the characteristics of the heat and mass transfer in bubbling flows. Bubble motion in bubbling processes has, for the most part, been inferred from idealized flow events such as single bubble formation and the rise of single or pairs of bubbles. For turbulent bubbling processes, little has been done so far experimentally or numerically to elucidate the relative importance of each such bubbling event in arbitrary bubbly-jet processes, and the mechanisms promoting or suppressing certain sequences of events. The behavior of deformed and spherical bubbles differs significantly in terms of alignment and dispersion: deformed bubbles could be associated with significantly different flow structures as compared to spherical bubbles, but modified energy decay due to pseudo-turbulence is ubiquitous (Bunner and Tryggvason, 2003). Differences in the bubbling can affect the turbulent structure throughout the multi-phase flow. Based on the database analyses of van den Akker (1998), "phase locking" was proposed as a possible cause of coherent structure generation, and an analogy was drawn between the von Karman vortex sheet behind a blunt body and the staggered arrangement of vortices in the liquid phase on either side of a meandering bubble plume.

A feature of the flow in bubbling processes that has been neglected to date is bubble break-up. In a study of the oscillation and break-up of bubbles in a turbulent field in micro-gravity, Risso and Fabre (1998) demonstrated turbulence to be potentially responsible for the deformation and break-up of individual bubbles. Kolev (1993) reviewed

* Corresponding author. Tel.: +41 44 6327073; fax: +41 44 6331662.
E-mail address: lakehal@iet.mavt.ethz.ch (D. Lakehal).

0142-727X/$ - see front matter © 2006 Elsevier Inc. All rights reserved.
doi:10.1016/j.ijheatfluidflow.2006.03.003

the numerous models for bubble break-up, in particular those based on a force balance between shear stress around the bubble and surface tension. The force balance concept forms the basis of the theory of Kolmogorov–Hinze (Kolmogorov, 1949; Hinze, 1955), postulating a critical Weber number for bubble break-up. The theory identifies resonance oscillation, in which eddy excitation and bubble oscillation are in phase, as an additional mechanism for bubble break-up. Martinez-Bazan et al. (1999a,b) injected air bubbles into fully developed turbulent water flow, and measured the resulting bubble size probability density function (p.d.f.). Bubble break-up frequency was determined as a function of bubble size and a critical diameter, depending on the surface tension and the dissipation rate. Break-up frequencies were shown to scale differently for large bubbles, as compared to bubbles sized in the order of the critical diameter. This result led to the identification of two distinct bubble size regimes.

A common feature of the studies discussed above is that turbulence is active in the liquid phase flow only, because the dispersed phase is formed by small size bubbles. Thus, extending the relevance of these studies to large-scale bubbling processes cannot be justified. Liquid-side turbulence in bubbly flow is important (for mixing) in regions far away from the source of bubble generation, where upstream flow events such as bubble formation and detachment can be ignored. In reality, vigorous break-up of large bubbles is a precursor to idealized bubbly flow. Additionally, in the case of bubbling processes, the establishment of a turbulent liquid-side flow is necessarily the result of a turbulent jet flow from the pipe. Interface–turbulence interactions and the physics involved in the break-up process are poorly understood. The description of bubbling by means of simplified models for bubble formation, bubble-rise and break-up will not properly represent the reality of the process.

In this paper, we introduce a new LES approach for interfacial, turbulent multi-fluid flows, based on the filtered single-fluid Navier–Stokes equations, in which the super-grid interface kinematics and turbulence are fully resolved. The description is more detailed than in the original contribution of Liovic et al. (2004). To the best of our knowledge, this study represents a first attempt at capturing gas-side turbulence and interface/turbulence interactions, knowing that at this stage it is impossible to resolve the entire spectrum of turbulence and interfacial deformation scales. LES is therefore adopted for capturing turbulence within the framework of the single-fluid formalism. We first introduce the filtered governing equations within the single-fluid formalism, and the resulting sub-grid scale terms that need to be modeled. Our main purpose is to address the predictive capability of a combined interface tracking/LES approach to understand some subtle facets of interface–turbulence mechanisms. The method is applied to a specific turbulent large-scale bubbling process. Results are discussed and compared to the available data from the experiment of Meier (1999) and Meier et al. (2000).

2. Numerical method

2.1. The primitive one-fluid equations

For flows consisting of immiscible fluid parcels of length scales larger than the grid size, phase inter-penetration is not presumed. Rather, jump conditions between the two phases are directly incorporated, such that the separate equations for each phase k can be replaced by a single set of equations describing the system. This is the starting point of the simplification from a multi-field to a single-field representation of the flow, in which the phases are identified locally using the indicator (or *color*) function C. In the continuous limit, color function C is the Heaviside function

$$C(\mathbf{x},\mathbf{t}) = \begin{cases} 1 & \text{if } \mathbf{x} \text{ occupied by phase } k = G, \\ 0 & \text{if } \mathbf{x} \text{ occupied by phase } k = L \end{cases} \tag{1}$$

such that the C-weighted local density defined by

$$\rho \equiv \sum_k C^k \rho^k = C\rho^{\mathrm{G}} + (1-C)\rho^{\mathrm{L}} \tag{2}$$

reduces to liquid density ρ^{L} or gas density ρ^{G}. The color function C helps describe the interface motion by the topology equation:

$$\frac{\partial C}{\partial t} + \mathbf{u}_{\mathrm{i}} \cdot \nabla C = 0, \tag{3}$$

where the interface velocity $\mathbf{u}_{\mathrm{i}}$ reduces in the non-phase change case to the local fluid velocity $\mathbf{u}$.

Further, separate species mass conservation equations can then be described using the local density ρ:

$$\frac{\partial \rho}{\partial t} + \frac{\partial}{\partial x_j}\rho u_j = 0. \tag{4}$$

Since the fluids are taken to be incompressible, the density of a fluid particle is constant along its trajectory ($\mathrm{D}\rho/\mathrm{D}t = 0$). This suggests that the mass conservation of the system (4) can be represented by the combination of the continuity equation, $\nabla \cdot \mathbf{u} = \mathbf{0}$, and the topology equation (3). This is valid as a statement of volume conservation in the single-fluid representation of multi-phase flows. Detailed derivation of the mass conservation in this context has been presented by Lakehal et al. (2002a).

For momentum conservation, we propose a local viscosity μ that similarly takes the form of Eq. (2), i.e. $\mathrm{D}\mu/\mathrm{D}t = 0$. The constitutive relation between the rate-of-strain tensor S_{ij} and viscous stress tensor σ_{ij} presumes both fluid species to be Newtonian, i.e.

$$\sigma_{ij} = 2\mu S_{ij} \quad \text{with} \quad S_{ij} = \frac{1}{2}\left(\frac{\partial u_i}{\partial x_j} + \frac{\partial u_j}{\partial x_i}\right). \tag{5}$$

The single-field momentum equations may thus be written as

$$\frac{\partial(\rho u_i)}{\partial t} + \frac{\partial}{\partial x_j}\rho u_i u_j = -\frac{\partial p}{\partial x_i} + \frac{\partial \sigma_{ij}}{\partial x_j} + \rho g_i + \gamma\kappa\hat{n}_i\delta. \tag{6}$$

The surface tension term here is $\gamma\kappa\hat{n}_i\delta$, where γ is the surface tension coefficient, κ is the interfacial curvature, $\hat{n}_i$ is the unit interface normal, and δ is the surface delta function. Finally, p denotes the incompressible total pressure.

2.2. The filtered one-fluid equations

2.2.1. The component-weighted volume averaging (CWVA) procedure

The one-field equations (Eqs. (2)–(6)) are a micro-scale, primitive description of immiscible, incompressible, Newtonian two-phase flow. The macro-scale description (at the super-grid level) of the flow suggests all dependent variables contain sub-grid scale (SGS) components $f' = f - \bar{f}$, where the resolvable quantities $\bar{f}$ are obtained by convolution using a spatial filter G:

$$\bar{f}(\mathbf{x},t) \equiv G \otimes f = \int_D G(\mathbf{x}-\mathbf{x}')f(\mathbf{x}',t)\mathrm{d}\mathbf{x}', \tag{7}$$

verifying the normalization property

$$\int_D G(\mathbf{x}-\mathbf{x}')\mathrm{d}\mathbf{x}' = 1. \tag{8}$$

The filtered phase indicator function,

$$\overline{C}(\mathbf{x},t) \equiv G \otimes C = \int_D G(\mathbf{x}-\mathbf{x}')C(\mathbf{x}',t)\mathrm{d}\mathbf{x}', \tag{9}$$

is subsequently interpreted as a volume fraction indicator function. This is the exact definition of the volume-of-fluid (VOF) quantity. The derivation of the filtered one-fluid equations is based on the use of the component-weighted volume averaging (CWVA) procedure (Lakehal et al., 2002b). In the filtered two-fluid formulation of the momentum equations derived by Lakehal et al., the separate solutions generated for each phase k were weighted in inter-penetrating-phase regions by the resolved volume fraction. In the single-field description of the flow, the coupling of $\overline{C}$ to the flow solution is instead represented through the local density (Eq. (2)). Therefore, as a basis for CWVA in the single-field formulation, it is most appropriate to use the local density ρ, which in essence is analogous to Favre averaging for compressible flows:

$$\tilde{f}(\mathbf{x},t) = \frac{\overline{\rho(\mathbf{x},t)f(\mathbf{x},t)}}{\overline{\rho(\mathbf{x},t)}}. \tag{10}$$

2.2.2. The filtered single-fluid conservation equations

Before proceeding further, it is perhaps useful to bring in the following conceptual clarification: In the single-fluid formalism for incompressible, isothermal multi-phase flows, the mass conservation of the system is described by both the continuity equation ($\nabla\cdot\mathbf{u}=\mathbf{0}$) and the topology equation (3).

In using CWVA in this context, the property according to which filtering and differentiation commute can be extended to the multi-fluid flow context, too, provided the discretization is performed over uniform meshes. Applying relation (7) to the local density yields

$$\begin{aligned}\bar{\rho}(\mathbf{x},t) &\equiv \sum_k \overline{C^k(\mathbf{x},t)\rho^k} \\ &= \overline{C}(\mathbf{x},t)\rho^{\mathrm{L}} + (1-\overline{C}(\mathbf{x},t))\rho^{\mathrm{G}}.\end{aligned} \tag{11}$$

For mass conservation, filtering of Eq. (4) via relation (7) then performing CWVA (10) yields

$$\frac{\partial\bar{\rho}}{\partial t} + \frac{\partial}{\partial x_j}\bar{\rho}\widetilde{u_j} = \varepsilon_{\mathrm{c}}^{\rho}, \tag{12}$$

where $\varepsilon_{\mathrm{c}}^{\rho}$ denotes the commutation errors, which will be neglected hereinafter.

Equating Eq. (11) into the filtered mass conservation equation above allows the filtered topology equation to be written in the form:

$$\frac{\partial\overline{C}}{\partial t} + \frac{\partial}{\partial x_j}\overline{C}\widetilde{u_j} = 0, \tag{13}$$

which unlike in the primitive formulation has now a conservative form. This is an interesting outcome compared to single-phase compressible Navier–Stokes equations where both the primitive (i.e. DNS) and LES mass conservation equations are conservative.

In typical incompressible finite-volume flow solver technologies, such as projection and SIMPLE-based solution algorithms, the coupling between momentum and mass conservation equations is generally achieved via some form of the pressure correction equation that features a $\nabla\cdot\mathbf{u}$-type source term. To extend this feature to the LES context, incompressibility of the fluids can be assumed, in which case the filtered density should, like in the primitive formulation, remain constant along the fluid particle trajectory

$$\frac{\widetilde{\mathrm{D}}\bar{\rho}}{\mathrm{D}t} \equiv \frac{\partial\bar{\rho}}{\partial t} + \widetilde{u_j}\frac{\partial\bar{\rho}}{\partial x_j} = 0. \tag{14}$$

This obviously helps reduce the filtered mass conservation equation to a simple filtered continuity equation: $\nabla\cdot\widetilde{\mathbf{u}} = 0$. The validity of this assumption[1] is clearly grid dependent, and its use should be treated cautiously. However, since LES is by definition a dense grid, refined time simulation, the incompressibility assumption (14) can be safely made. It is indeed unlikely that a rigorous LES that is supposed to provide high-order turbulence statistics can be performed on a coarse grid on which the condition (14) is not fulfilled. To be coherent, however, this issue can be solved a posteriori, in the pressure correction equation, with scope for the entire mass residual ($\nabla\cdot\widetilde{\mathbf{u}} - \widetilde{\mathrm{D}}\bar{\rho}/\mathrm{D}t$) to be incorporated into the source term. In addition, the filtered topology equation should be solved under the conservative form above (13), which is the case in the present code (Liovic et al., 2006).

[1] We acknowledge the note raised by of the referees about this issue.

The divergence-free representation of both the primitive and the phase filtered velocity fields is neither true for high-speed isothermal flows nor for convective phase-change situations.

Performing the convolution product on the momentum equations and applying the local density-based CWVA (10) yields

$$\frac{\partial \bar{\rho}\widetilde{u}_i}{\partial t}+\frac{\partial}{\partial x_j}\bar{\rho}\widetilde{u}_i\widetilde{u}_j=-\frac{\partial \bar{p}}{\partial x_i}+\frac{\partial \widetilde{\sigma}_{ij}}{\partial x_j}+\bar{\rho}g_i+\gamma\bar{\kappa}\overline{\hat{n}_i}\delta \underbrace{-\frac{\partial \tau_{ij}}{\partial x_j}}_{\mathrm{I}}+\underbrace{\varepsilon_{\mathrm{c}}^{u}}_{\mathrm{II}}+\underbrace{\varepsilon_d}_{\mathrm{III}}+\underbrace{\varepsilon_\gamma}_{\mathrm{IV}}, \tag{15}$$

where we have made use of the identity

$$\varepsilon_d \equiv \frac{\partial}{\partial x_j}[\overline{\sigma}_{ij}-\widetilde{\sigma}_{ij}], \tag{16}$$

and introduced the local (phase-specific) SGS tensor, defined as

$$\tau_{ij} \equiv \bar{\rho}(\widetilde{u_i u_j}-\widetilde{u}_i\widetilde{u}_j). \tag{17}$$

Term II designates the sum of errors which appears if commuting between the filtering and differencing operators were not assumed explicitly. Term III represents the inter-phase net force between the two fluids at the sub-grid level. It could represent the drag and lift forces for a bubble of a diameter smaller than the filter width. Similar to ε_d, the last term (IV) appears as a non-linearity error, which vanishes away from the interface, i.e.

$$\varepsilon_\gamma = \gamma\overline{\kappa\hat{n}_i}\delta-\gamma\bar{\kappa}\overline{\hat{n}_i}\delta. \tag{18}$$

It denotes the non-resolved counterpart of surface tension, which has been washed out by filtering. The SGS modeling of non-resolved interfaces is less clear than that of the non-resolved turbulence. In turbulence, the smallest length scale of the problem is the Kolmogorov length scale. In contrast, the non-resolvable interfacial scales are difficult to characterize, even if there exists an approximate scale based on the critical length (l_c) determined from the balance between surface forces and local turbulence intensity. However, the main reason for not modeling the SGS interfacial scales is that the super-grid surface tension force itself cannot be computed accurately enough with current schemes. Surface tension discretization schemes often lead to parasitic currents – a non-physical numerical forcing that, in a range of multi-phase flows, can be as great a contribution to a velocity-field update as advection-scheme numerical dissipation. In other words, it does not suffice to again split the curvature or the normal vector into resolved and SGS components – ultimately giving rise to extra unresolved quantities – before clarifying the interaction mechanisms between non-resolved turbulence and non-resolved interfacial scales.

2.3. SGS modeling

In the present study, centered differencing is used for momentum advection, and stability is preserved with the help of the dissipation contribution from explicit SGS modeling. The standard Smagorinsky-kernel-based SGS model was employed using a value of the damping constant $C_s = 0.1$ – a value inferred from earlier LES computations of a turbulent bubbly flow by Lakehal et al. (2002b) using the dynamic approach (DSM) of Germano et al. (1991). The DSM approach could not be used because, in contrast to mixing layers and wall bounded-flows, there is no homogeneous direction over which the constant C_s could be averaged in bubbling processes. Three-dimensional averaging of C_s would lead to very small values because turbulence is essentially concentrated in the bubbling region, as will be shown later. Turbulence near-wall damping was achieved by incorporating the van Driest expression into wall functions. Note finally that for interfacial flows separated by well-defined continuous fronts, any well-established SGS model for single-phase flow could be applied, since the Reynolds stresses are density-weighted for each phase. Both the class and width of the space filter could vary from one phase to the other, too. Models more elaborate than eddy viscosity-based SGS models could also be employed, including, for example, those based on the deconvolution principles. However, the fact that the lighter phase perceives interfaces as evolving rigid boundaries (Fulgosi et al., 2003) suggests that a near-interface treatment is required, in a similar manner to wall flows. Interface functions are thus needed, which could be incorporated into models based on distance function about the interface.

2.4. Numerical schemes

2.4.1. Interface tracking

Vigorous bubbling imposes special requirements for interface tracking methods, in that any particular method must robustly and accurately capture all stretching, fragmentation and coalescence phenomena induced by gas injection. The range of interface length scales and high-curvature interfaces generated in bubble break-up, liquid elongation, bubble coalescence and other phenomena represent a major challenge to particle-based and level-set methods, in that rigorous local volume conservation becomes necessary, and the breaking of a closed surface into multiple closed surfaces must be captured. Ultimately, volume tracking (VOF methods) based on piecewise planar interface reconstruction (commonly known as PLIC-VOF (piecewise linear interface calculation) (Rider and Kothe, 1997) is currently the best interface tracking scheme for robustly and accurately tracking the kinematics, creation and destruction of all resolvable interfaces in such flow problems. In the implementation used here, the 3D PLIC-VOF scheme features piecewise planar interface reconstruction based on the Youngs' (1982) gradient, and uses direction splitting to extend one-dimensional flux updates to 3D (i.e. a three-step update of $\overline{C}$). With this scheme, bulk-property distributions such as density and viscosity are geometrically extracted from the interface

reconstructions. The location of the interface described by the color function is used to model surface tension, using a fully kernel-based variant of the continuum surface force (CSF) method of Brackbill et al. (1992).

2.4.2. Other numerics and code issues

Meaningful LES requires long computational times, and as such simulating all the transients in interface tracking-based LES requires adequate computing power. The computer code employed here simulates transient 3D flows in complex geometries on distributed-memory platforms, with MPI-facilitated parallelism based on domain decomposition. The flow solver is based on a standard projection method and second-order Euler time-stepping (Liovic et al., 2002). Using domain decomposition, the computation is sub-domain-based, thus helping achieve scalable parallel performance. An additional contribution to scalable parallel performance is provided by a Krylov subspace-based Poisson solver featuring Additive Schwarz pre-conditioning, in which rudimentary interface conditions between sub-domains are used in order to minimize interprocessor communication.

3. Air venting through a downward-facing pipe

In the bubbling process investigated here, air is vented downwards through a vertical pipe into a water bath (Fig. 1). The pipe is referred to as a "downcomer" in the thermal hydraulics lexicon and as a "lance" in extractive metallurgy. Previous to this work, Hirt and Nichols (1980) had considered this problem with a weak-compressibility hydrodynamics solver, but as a demonstration application, without providing insight into the phenomena and physics of the flow. In more recent studies, Meier et al. (2000) and Liovic et al. (2002) have had success in predicting this class of flow using VOF under laminar flow conditions. This flow has been deliberately selected for having dual dynamical aspects: the inertia-dominated jetting from the pipe tip is in the opposite direction to the buoyancy force associated with free bubble rise, such that the prevailing flow physics can be distinguished to a substantial extent. From the turbulence point of view, the presence of the pipe wall results in shear flow that is further complicated by the dynamics associated with a highly deformable interface. From the interface dynamics point of view, the presence of the pipe obstructing the detachment and rise of formed bubbles results in a variety of phenomena, e.g. instability of annular bubbles and the formation of vortex rings taking the form of "mushroom-cloud" bubble inversions (Meier, 1999).

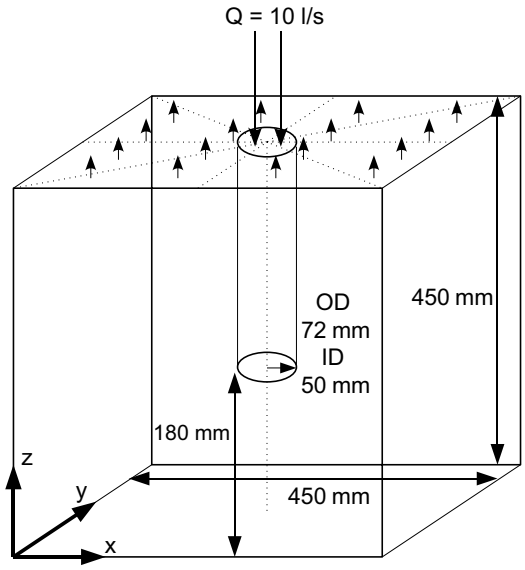

Fig. 1. Setup of the computational domain.

3.1. Problem setup

To conform with the experiments performed by Meier et al. (2000), the computational domain of height and breadth 450 mm (Fig. 1) was discretized using an orthogonal, non-uniform 64^3 mesh. The pipe (inner diameter 50 mm, outer diameter 72 mm), was centrally located, with its tip 180 mm above the bottom of the domain. The *xy*-plane (where *z* is vertical) was refined in a "core bubbling" region (225 mm × 225 mm) using spacing corresponding to a 96×96 mesh, and the pipe diameter was resolved by 10 cells. Except for the inflow area, the top boundary was represented as an outflow boundary. Free-slip boundary conditions were applied to the bottom surface and to the vertical planes of the domain.

In the present study, air venting occurs at 10 l/s, and is not choked i.e. the injection flow rate is constant. This is a particular case documented by Meier et al. The Reynolds number of the pipe flow is 17,000. Within the range of air venting flow rates considered in Meier's experiment, the 10 l/s case represents a transition between lop-sided and symmetric bubble rise, as well as between laminar and turbulent gas-side flow. Gaussian perturbations were superimposed on the initially quiescent bulk flow, providing a turbulence intensity of 0.5% relative to the mean inflow velocity. Simulations were performed on a 16-CPU parallel computer, using a Courant number of 0.2 and signal sampling at 1000 Hz.

3.2. Transient large-scale bubbling phenomena

Fig. 2 shows sample snapshots of bubble interfaces captured during the simulation. For qualitative comparison, the figure also shows sample snapshots of bubble surfaces captured on video at the same flow rate. Noteworthy phenomena include almost symmetric bubble growth and rise, "fingering" of the upper bubble surface during rise, and lop-sided bubble detachment and free-rise. The simulation of the observed bubble fragmentation demonstrates the ability of VOF to robustly capture the most challenging interface kinematics in a realistic manner, even down to generating and preserving the satellite bubbles.

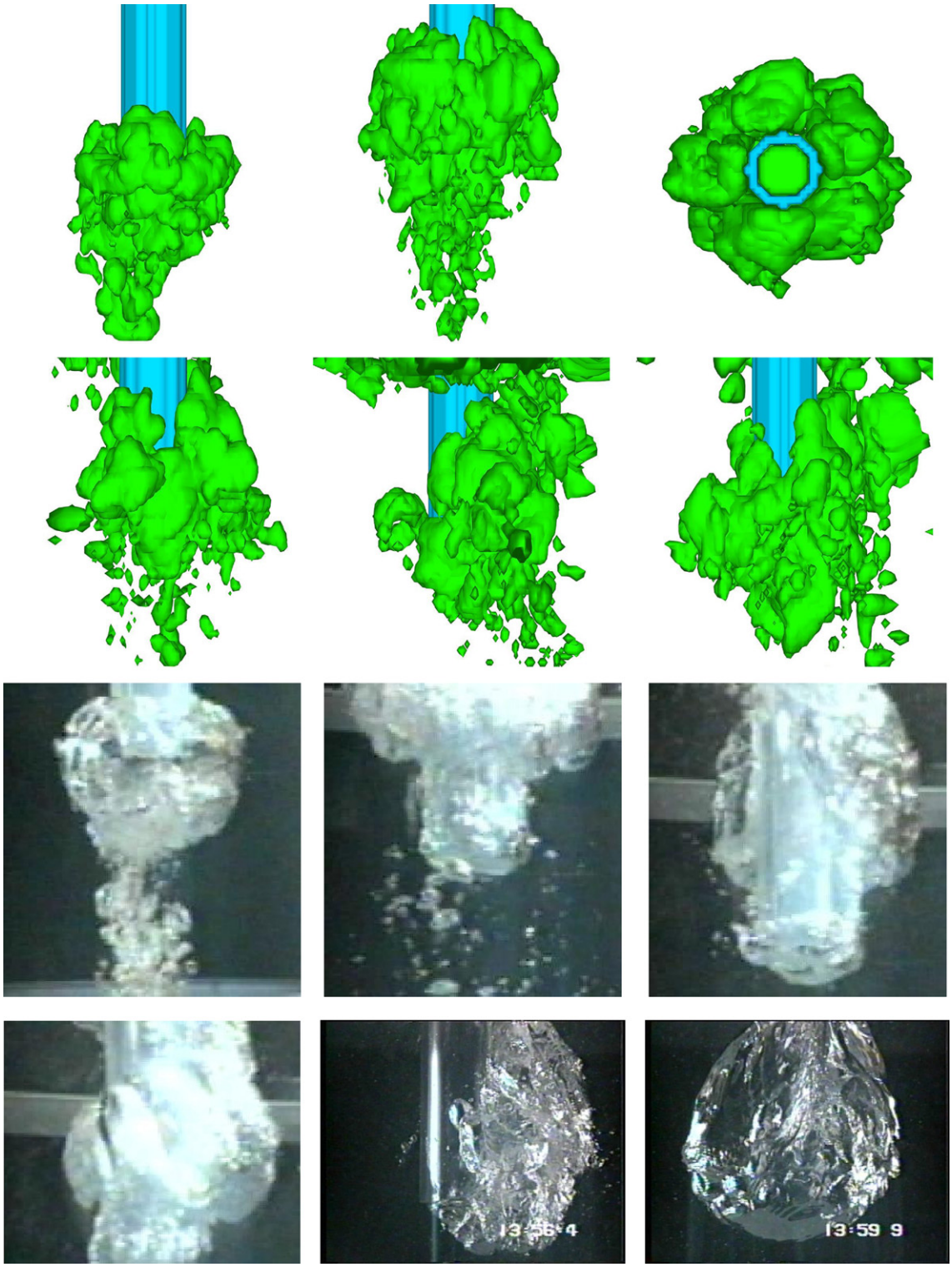

Fig. 2. Snapshots of the bubbling resulting from air venting through a downcomer, for air flowing at 10 l/s into a water bath. First and second rows: simulation; third and fourth rows: experiment (from the work of Meier, 1999). The first two experimental snapshots are within the time frame captured by simulation, while the other four snapshots are representative of steady-state operation.

From commencement of air venting, the snapshots presented in Fig. 2 correspond to a time interval of 1.1 s. Of the 10 l/s Meier experimental snapshots shown in the figure, the first two occur within the simulated time interval, while the others correspond to steady-state bubbling beyond this interval. Steady-state bubbling from the tip is established early on in the 1.1 s interval; by the end of the simulated interval, $O(10^1)$ bubbles have grown,

detached and risen away from the pipe tip. Beyond the growth of the first bubbles (start-up), the data within the envelope of the bubble plume is fairly representative of statistically steady flow. One feature of the flow within the initial 1.1 s interval that is not sustained into the long-term statistically steady flow is the presence of a low-concentration dispersion of entrained bubbles well below the bubble plume envelope of steady-state venting. Due to the surge of the first jet into an initially quiescent bath, this dispersion has little effect on the flow associated with the bubble plume above it, and the region deep below pipe tip is of little interest in the current study.

The transitional nature of the bubbling in the 10 l/s air flow-rate case is shown in Fig. 2. The first visible transition shown in the experimental frames is that between symmetric rise of the growing bubble and lop-sided rise. The second visible transition relates to interface wrinkle scales covering the majority of the bubble surface, with transition between smooth interface dominance and chopped-up interface dominance. The snapshots in Fig. 2 show that transition of both types is captured in both directions.

In the case of constant volumetric flow rate venting and away from the high-flow-rate end of the spectrum, Meier (1999) found bubble growth to exhibit less distinguishable growth/detach patterns, but rather a quasi-continuous escape of gas to the side. This lop-sidedness, faithfully captured in the simulation, was noted in the experimental work to be a factor that seriously complicates measurement of bubbling frequency. In such cases, pressure signal analysis was considered to be useless; bubble counting exclusively was used in experiment to determine the bubbling frequency in constant flow rate venting, and is therefore also used here. Table 1 shows the bubbling frequency extracted from the simulation to match the frequency captured in the experiment for air–water systems.

Given the nature of the video image database for the 10 l/s case (Meier, 1999), quantitative comparison for validation between simulation and experiment is best achieved using start-up data. Level measurements of the bubble upper surface, and the maximal spreading of the growing bubble away from the outer pipe wall at tip level were compared. Fig. 3 shows the time-history of the bubble upper surface level; the comparison is excellent over the entire time-history of start-up. In the comparison of the maximal spreading of the bubble plume, the simulation overestimated the spreading by 7% compared to measurements. The agreement between simulation and experiment using three different measures for quantifying bubbling, even at the current mesh resolution, is a strong validation of the numerical method applied to the bubbling problem under investigation. The level of the lower bubble surface is not appropriate for use in quantitative comparison here, because the extreme fragmentation from the lower bubble surface, due to the surge of the initial jet, is poorly resolved.

Table 1
Measurements generated from simulation and experiment of the 10 l/s air venting experiment of Meier (1999), during start-up and in the establishing of steady-state bubbling

	Simulation	Experiment
Tip-level spread – first bubble (mm)	48	45
Bubbling frequency (Hz)	7	7

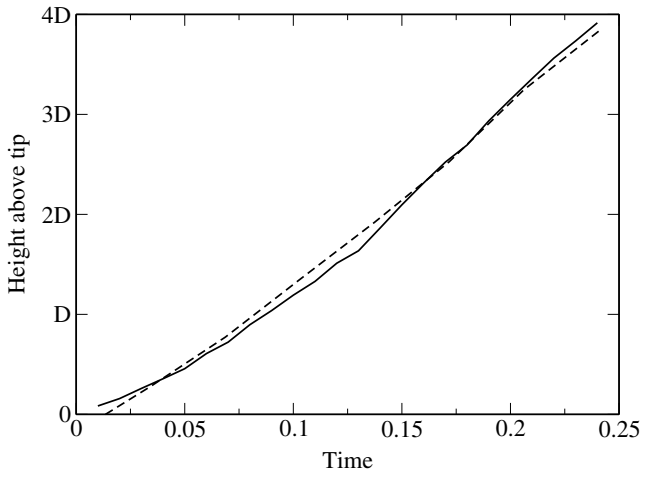

Fig. 3. Transient behavior of the level of upper bubble surface during start-up bubble formation and detachment for 10 l/s air venting: (---) refers to levels relative to the pipe tip obtained from the experiment, while (—) refers to results from the simulation. (Time in s.)

Another event observed but not documented here is the vigorous break-up of bubbles well above pipe tip level. This level is often at $\approx 5D_i$ above, where our characteristic length scale is the internal pipe diameter D_i. This break-up takes the form of a "mushroom-cloud" – an abrupt inversion and radial expansion of the bubble plume, and resembles bubble swarming, i.e. massive fragmentation into smaller bubbles. This bubble swarming is captured in simulation, but we ignore this aspect of the flow here because of the close proximity of the outflow boundary.

3.3. Interfacial area evolution

The interfacial area and bubble volume were computed in a sub-domain excluding flow zones located above $z = 0.35$ m, in order to avoid using unreliable sampling results in proximity to the outflow. Fig. 4 shows (a) the bubble interfacial area, (b) the bubble plume gas volume, and (c) the plume surface-area/volume ratio, for the duration of the simulation. After the growth of the initial bubbles, the surface area exhibits a cyclic variation about a mean value, followed by a second surge near the end of the time interval. Large bubble volumes are seen to result from the more symmetric bubble growth events seen in Fig. 2, while the other peaks coincide with more lop-sided bubble growth scenarios. Resemblance between the interfacial area signal and the bubble volume signal is apparent, with maxima, minima and inflections shown to be in phase and of similar magnitude relative to the maxima of the first

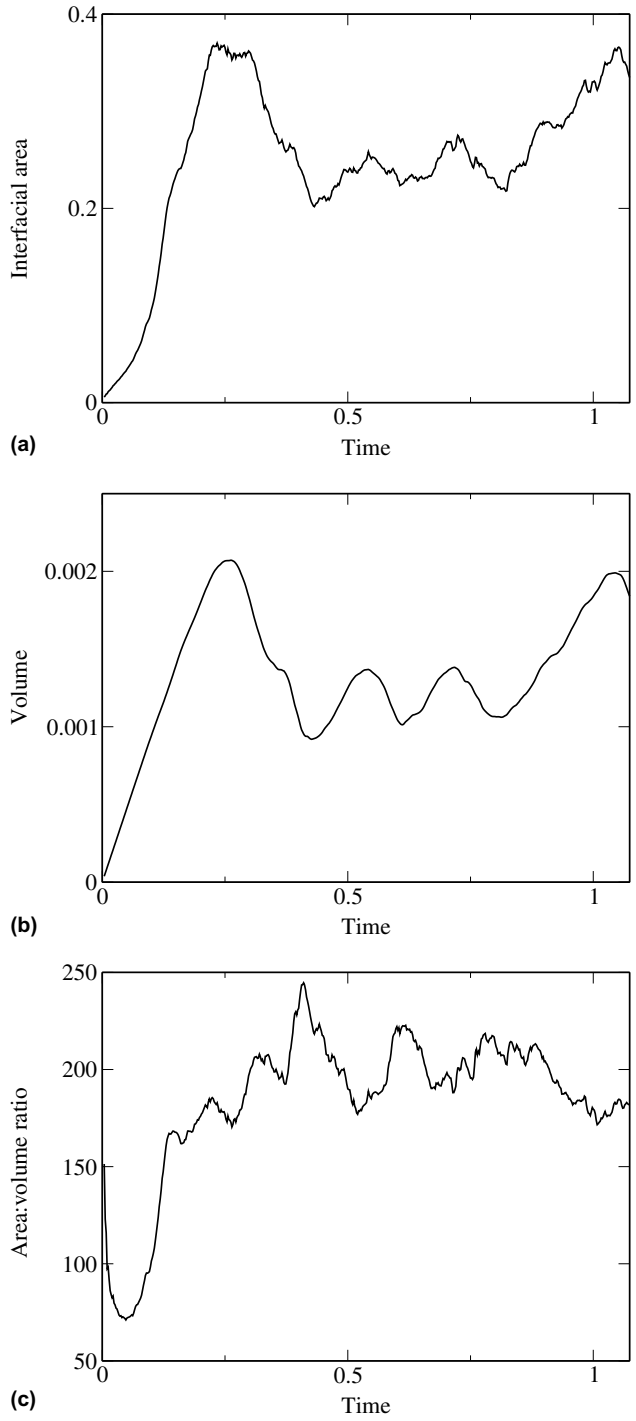

Fig. 4. Time signals of bubble plume interfacial area, bubble plume volume, and the interfacial-area/volume ratio. The domain over which the volume and surface integrals are included is restricted, with the top 20% of the domain neglected to avoid contamination of results with near-outflow-boundary interface data. (Time in s, area in m^2, volume in m^3.)

bubble. The interfacial area signal shows significant low-amplitude noise, as compared to the bubble volume signal.

The surface-area/volume ratio is at its lowest level in the early stages, when a smooth-surfaced single growing bubble prevails. Upon the establishment of steady-state conditions, the ratio converges to an average of approximately 200:1, with a relatively low standard deviation. Normalizing with the surface-area/volume ratio for a spherical bubble of constant diameter, this average value corresponds to a dispersion of spheres of diameter $\approx 6\bar{\Delta}$. Length $\bar{\Delta} = (\delta x\,\delta y\,\delta z)^{1/3}$ can be interpreted as the average resolvable length scale of the gas phase.

3.4. Interface/turbulence interactions

Fig. 5(a) shows a profile through the axis of symmetry of the velocity vector map and interface location at a particular instant during the 10 l/s simulation. The interaction between the interface and the large-scale structures formed in the gas phase well illustrated. One form of such interaction is the formation of distinct lobes. Another feature shown by Fig. 5(a), and even more clearly by Fig. 5(b) (taken from a 16 l/s simulation on a 96^3 mesh), is the existence of high-shear flow zones, that we have deduced to lay between the structures of the distinct lobes. High vorticity values shown in Fig. 6(a) are concentrated in the gas-side flow in the vicinity of the pipe tip, and some of the highest regions of vorticity indeed coincide with high-shear flow zones.

From comparing the 2D center-plane plot of vorticity in Fig. 6(a) to the corresponding interface profile of Fig. 5(a), a damping of vorticity can be seen as the interface is

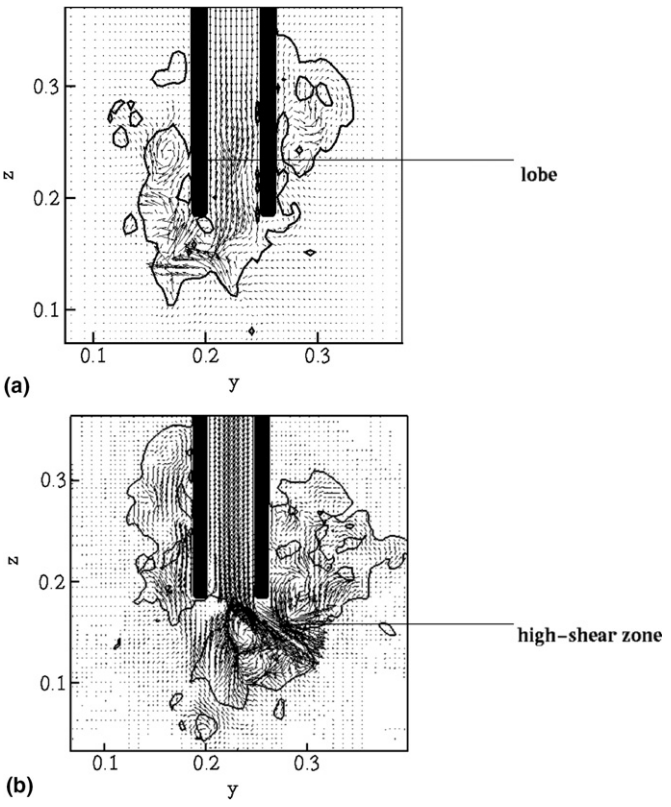

Fig. 5. Plane interface locations and velocity vector maps at different instants: *yz*-plane for (a) 64^3 resolution; (b) 96^3 resolution at a different flow rate (16 l/s). (Axis lengths in m.)

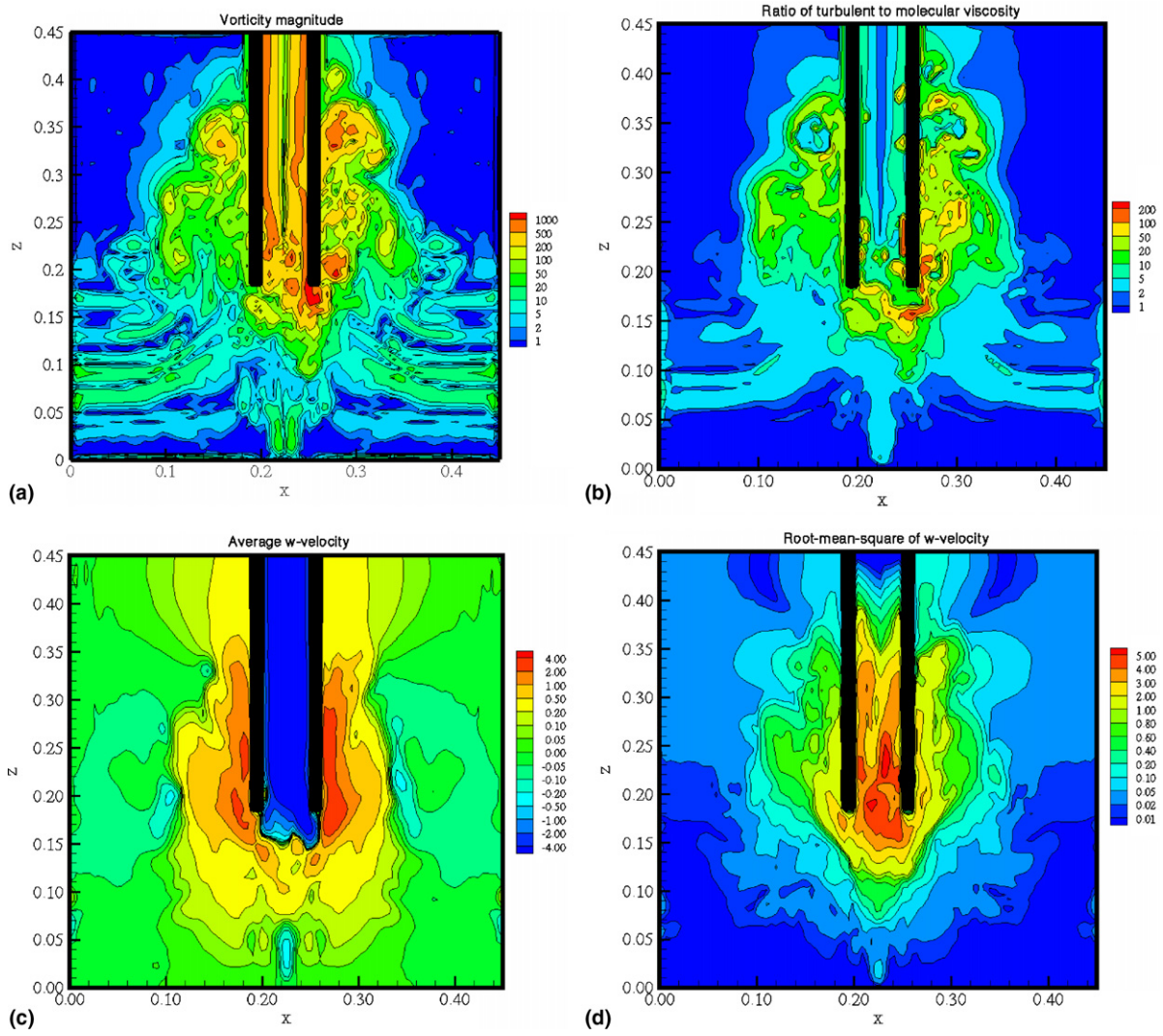

Fig. 6. Instantaneous and time-averaged yz-plane distributions: (a) vorticity magnitude, and (b) μ_T/μ, at $t = 0.23$ s; (c) time average w-velocity, (d) root-mean-square w-velocity.

approached from the gas side. This observation is consistent with conclusions drawn from DNS of counter-current stratified flow of Fulgosi et al. The contribution of the eddy viscosity from the SGS model, μ_T, to the total viscosity distribution, reveals that higher values coincide with high-vorticity gas-side flow regions. Locally higher values of μ_T in Fig. 6(b) informs that the portion of the spectra washed out as a consequence of under-resolution of turbulence coincides with the high eddy-viscosity regions. The Smagorinsky SGS model used in the present work is also known to be overly dissipative and not to accommodate backscatter of energy, and is one contribution to the possibly high magnitudes of μ_T. The value of the ratio μ_T/μ peaks in the 100–200 range in the high-shear region below the pipe, as indicated by the arrow in Fig. 5(b), whereas in the rest of the domain around the injection region, it lies within an acceptable (in the LES sense) interval range of 5–20. This result shows that the grid employed here is sufficiently fine to resolve most of the flow scales; a local grid refinement below the pipe tip (in the high shear zone) would help indeed provide a better resolution there.

Fig. 6(c)–(d) presents average and root-mean-square (rms) results of downward velocity in the yz-plane through the center of the pipe. The degree of asymmetry in these time-averaged results indicates that the actual simulation interval of 1.1 s does not provide a satisfactory approximation to a long-time average (compared to the LES of single-phase channel flow, for example), and suggests the need for even more computations to completely average out the asymmetries. The most intense velocity fluctuations are in the bubbling-jet area under the pipe tip, while a second area at about $5D_i$ above the pipe tip coincides with the mushroom-cloud region. More generally, areas of more intense velocity fluctuations coincide with the bubble plume, with gas-side turbulence intensity substantially greater than in the liquid. Away from the bubble plume, both in the pipe flow and the liquid-side flow, turbulence is low. Velocity fluctuations are an order of magnitude

smaller in the liquid-side flow as compared to the gas-side flow, and μ_T/μ are O(10)–O(10^2) smaller.

3.5. Coherent structures

The presence of the pipe and the gas-liquid interfaces seen from the gas-side as rigid walls contribute significantly to vorticity generation in the flow. Vorticity may therefore not be useful for *coherent structure* (CS) identification in this flow, because CS-specific contributions to the vorticity may be obscured by the near-wall/interface flow. In Fulgosi et al. (2003), a range of different measures were used in an attempt to extract CS from flows featuring a well-defined deformable interface. Jeong and Hussain (1995) introduced a CS identification technique based on the negative eigenvalue of second-largest magnitude from the tensor $s_{ij}s_{jk} + r_{ij}r_{jk}$, where s_{ij} and r_{ij} are the rate-of-strain and vorticity tensors respectively. Referred to as the $-\lambda_2$ approach, it was found in various simulations to provide the most accurate and thorough identification of CS even in near-interface turbulent flow, and is used here.

Fig. 7(a) shows iso-surface visualizations of CS using the $-\lambda_2$ approach at three instants in time that are consecutive. The opaque iso-surfaces correspond to $\lambda_2 = -25{,}000$, which was found to optimally filter out non-CS vorticity. The bubble surfaces, indicated by the $\overline{C} = 0.5$ iso-surfaces, are made translucent so as not to obscure CS. The alignment of CS shape with lobes in the surface of the large bubble in rise about the pipe is obvious. Impressively, despite lobes being resolved by no more than 10 mesh cells, the use of $-\lambda_2$ allows specific CS such as hairpin vortices to be recognizable.

Within the bubble plume rising about the pipe, CS is more concentrated in the lower half – which is not surprising in view of the high intensity of vorticity in the inertial jetting area near the pipe tip. At a height of $2D_i$–$3D_i$ above the pipe tip, the second frame shows substantial CS within the uppermost surface of the rising bubble plume. By the last frame however, the bubble swarm is seen to rise further away from the pipe tip, and the CS dissipate gradually. The mushroom-cloud is clearly visible by the time of the last frame; the accompanying fragmentation results in smaller lobes in gas volumes trapped within large bubbles, as well as many bubbles of smaller size. More notably, however, small lobe/bubble formation has the effect of locally laminarizing the gas flow. Even if more nodes were available for better resolution, the proportion of void occupied by CS would be seen to dissipate through the bubble plume.

For comparison with the results of the $-\lambda_2$ approach, Fig. 7(b) shows the vorticity iso-surfaces of $\omega_z = -500$ and 500 at the same times as in Fig. 7(a). The ω_z-pair clearly displays counter-rotating vortical structures – providing virtually the same insight as from the neighboring panel (a). Note that the choice of $|\omega_z| = 500$ is qualitative: larger values filtered out too much structure, while lower values did not adequately decouple flow structures. Visualization with the enveloping bubble iso-surface shows the structures associated with the $|\omega_z| = 500$ cut-off, for the most part, to fully coincide with the lobes. In the inertial jetting area the coherent structures should have been seen within the large-scale lobes in the bubble surface, but vorticity iso-surfaces seem incapable of resolving these structures there. The use of vorticity iso-contours is seen here to be somewhat inferior to the $-\lambda_2$ approach for CS identification in this category of flow.

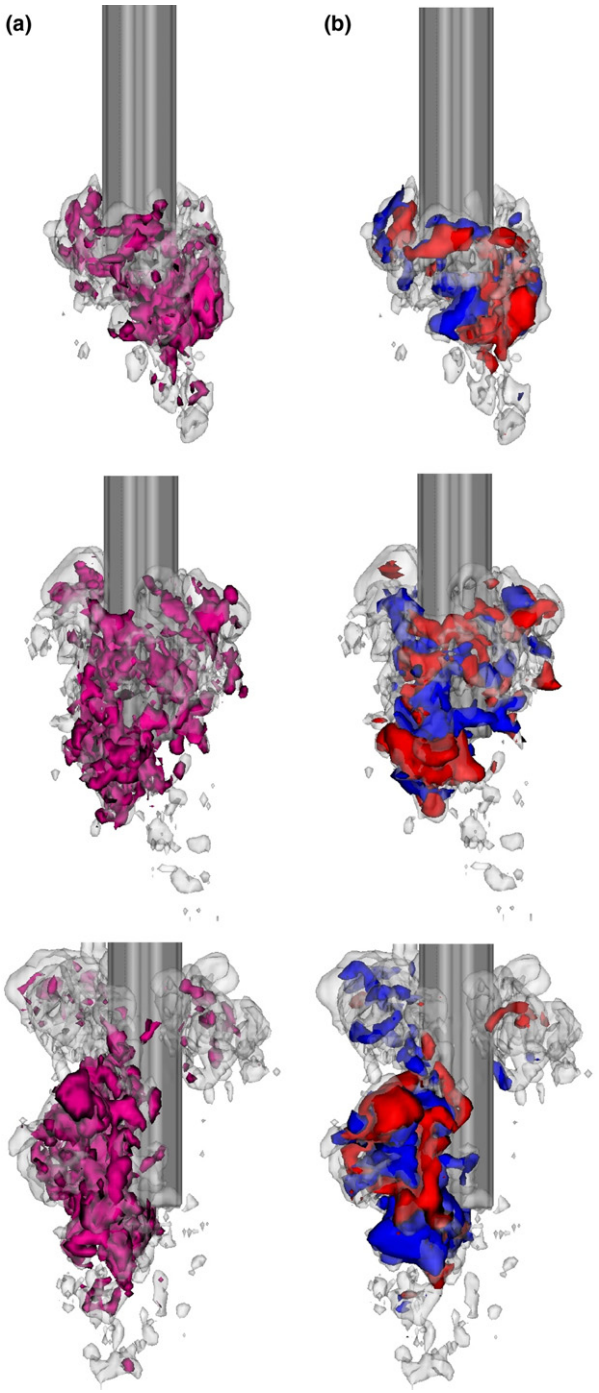

Fig. 7. Coherent structures within the gas-side flow at $t = 0.15$ s (top row), $t = 0.25$ s (middle row), and $t = 0.35$ s (bottom row), after the commencement of the bubbling simulation: (a) the iso-surface of $\lambda_2 = -25{,}000$, and (b) the iso-surfaces of the $-500/500\omega_z$ vorticity pair.

3.6. Azimuthally-averaged results

To characterize the plume boundaries about the downcomer as a function of distance from the pipe axis, the time-averaged results in 3D Cartesian space are averaged azimuthally in the xy-plane about the axis. A list of radial distances is created, and a minimum one-mesh-cell thick support of cells is flagged about each radial distance. Once the support of cells about any target radius, δ, is identified, an inverse distance-based interpolation is used to generate an azimuthally-averaged value. As an example, an azimuthally-averaged value of the void fraction, $\overline{\langle C \rangle}$, is determined by

$$\langle C \rangle = \frac{\sum_{(i,j,k)\epsilon\delta} w_{i,j,k} C_{i,j,k}}{\sum_{i,j,k\epsilon\delta} w_{i,j,k}}, \tag{19}$$

where

$$w_{i,j,k} = \frac{1}{|\mathbf{x}_{i,j,k} - \mathbf{x}_{r,\theta}|^p} \tag{20}$$

with $p = 1/2$ being used for smoothness of the profiles. In the present study, two xy-slices are analyzed – one slice at a distance of $0.45D_i$ below the pipe tip, and the other slice at a distance of $0.9D_i$ above the downcomer tip.

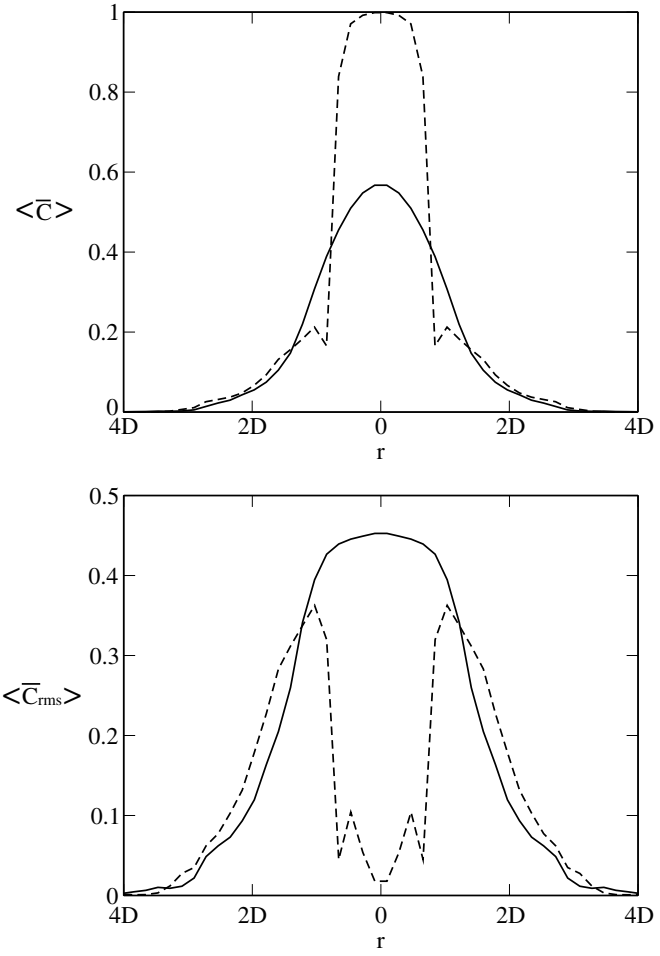

Fig. 8. Azimuthally-averaged radial profiles of $\overline{C}$ and $\overline{C}_{rms}$: (—) refers to the xy-plane at a distance of $0.45D_i$ below the downcomer tip, and (---) refers to the xy-plane at a distance of $0.9D_i$ above the downcomer tip.

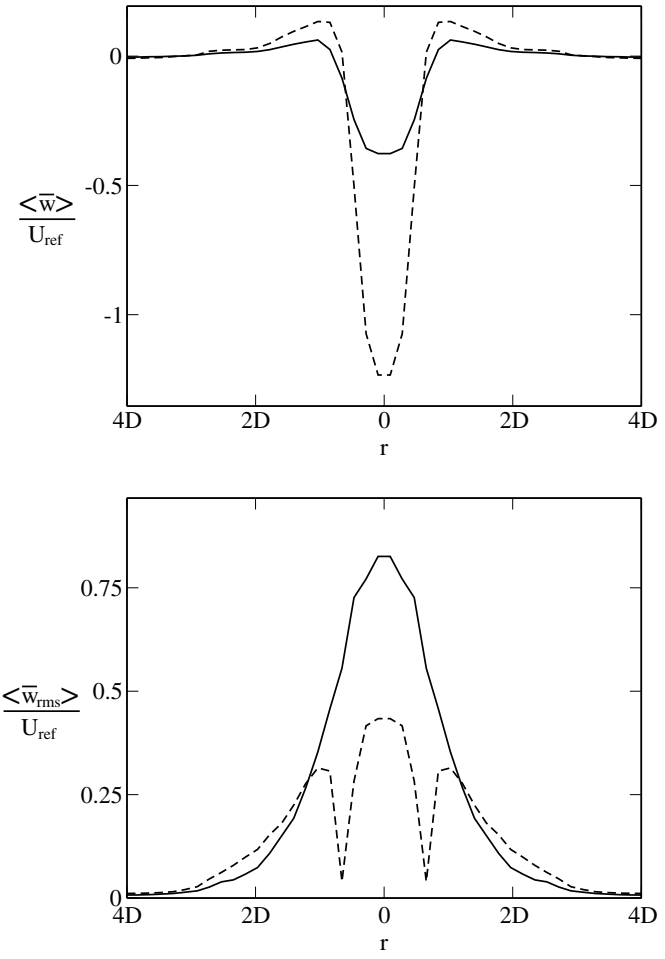

Fig. 9. Azimuthally-averaged radial profiles of $\overline{w}$ and $\overline{w}_{rms}$: (—) refers to the xy-plane at a distance of $0.45D_i$ below the downcomer tip, and (---) refers to the xy-plane at a distance of $0.9D_i$ above the downcomer tip.

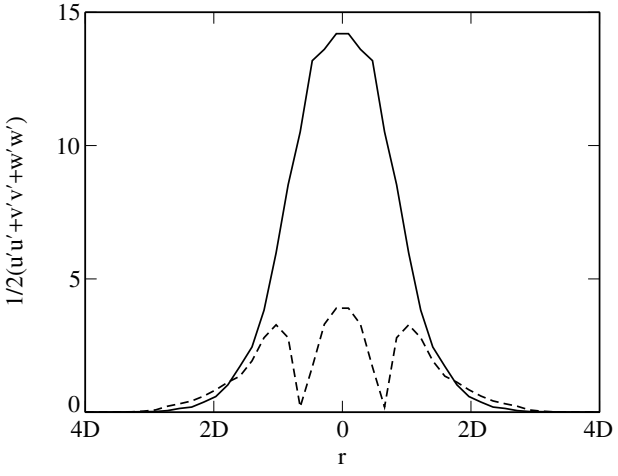

Fig. 10. Azimuthally-averaged radial profiles of turbulent kinetic energy: (—) refers to the xy-plane at a distance of $0.45D_i$ below the downcomer tip, and (---) refers to the xy-plane at a distance of $0.9D_i$ above the downcomer tip (TKE in $m^2\,s^{-2}$).

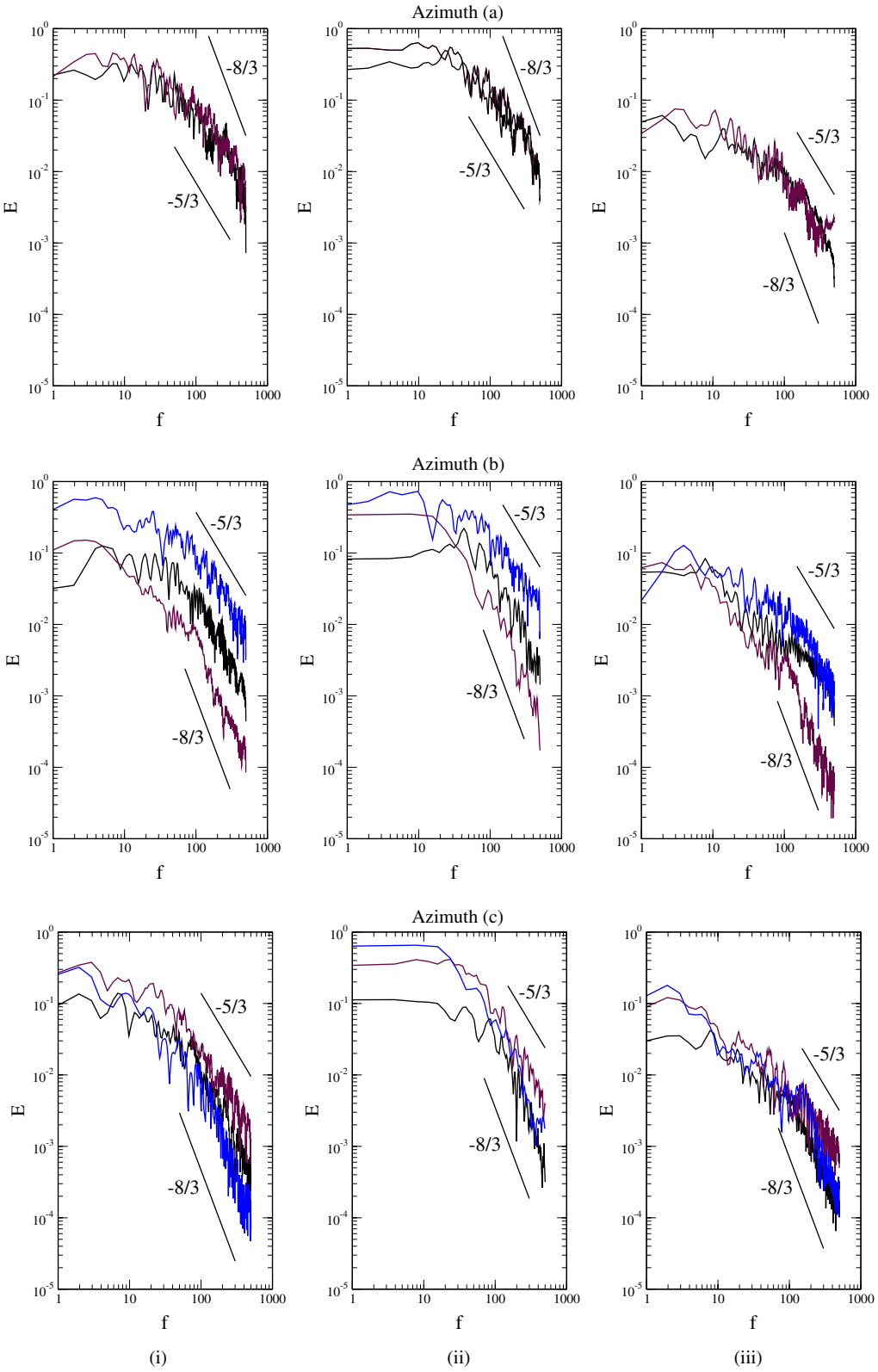

Fig. 11. Energy spectra for azimuth (a) – top row – $0.9D_i$ below tip, $0.4D_i$ off-axis, azimuth (b) – second row – $0.9D_i$ below tip, $1.3D_i$ off-axis, and azimuth (c) – third row – $0.9D_i$ above tip, $0.9D_i$ off-axis. Columns show representative point spectra of phase-independent signals (i), gas-specific signals (ii), and liquid-specific signals (iii), respectively. Use was made of the color function C to distinguish gas flow events from liquid flow events.

Fig. 8 shows the radial profiles of the average and rms of the void fraction, $\overline{\langle C \rangle}$ and $\langle C \rangle_{\mathrm{rms}}$. For the curves corresponding to the plane below the tip, the pipe does not intersect the plane, such that both the average and rms

distributions are continuous and smooth. The major difference between the average and rms curves of $\overline{C}$ is that the average curve features a bell-shaped distribution, while the rms profile exhibits a much broader peak. The curves corresponding to the plane above the tip show clear delineations between the flow in the bubble plume and the downward pipe flow. It can be seen that the bubble plume is slightly broader in the plane above the gas tip, and the rms fluctuations in void fraction are more intense – consistent with bubble rise through the plane. There is also a reduction in bubble plume void fraction adjacent to the outer pipe wall, and a more pronounced reduction in rms.

Fig. 9 shows the radial profiles of the average and rms of the w-velocity, $\overline{\langle w \rangle}$ and $\langle w \rangle_{\mathrm{rms}}$, scaled by the mean gas inflow velocity. For both planes considered, the mean vertical velocity is upwards in the region beyond the pipe radius; the profiles look similar, albeit with higher velocities for the plane above the tip, which was to be expected from the bubble acceleration up the plume. The downward velocity profile in the plane above the tip corresponds to the pipe flow. The profile in the plane below the pipe tip is dilated in the region beyond the outer pipe diameter by lateral spread of the jet, and the w-velocity fluctuations are high in the jetting region. Finally, Fig. 10 shows the turbulent kinetic energy profile in the same planes, confirming that the turbulence is concentrated in the gas-side flow with particularly high-intensity in the jetting region below the pipe tip.

3.7. Energy spectra and dissipation

The spectra shown in Fig. 11 were obtained by velocity signal recording for sample points in selected azimuths about the pipe axis. Azimuth (a) corresponds to a ring $0.9D_{\mathrm{i}}$ below the pipe tip and $0.4D_{\mathrm{i}}$ off-axis, azimuth (b) corresponds to $0.9D_{\mathrm{i}}$ below the tip and $1.3D_{\mathrm{i}}$ off-axis, and azimuth (c) corresponds to $0.9D_{\mathrm{i}}$ above the tip and $0.9D_{\mathrm{i}}$ off-axis. Signals at 16 equally-spaced points were recorded in each azimuth, as well as the spatial average. The columns identify spectra of signals that are: (i) phase-independent, (ii) gas-specific, and (iii) liquid-specific. The energy spectra of the azimuthally-averaged phase-independent signals (results not included here) reveal the existence of an inertial sub-range characterized by a $-5/3$ decay law that prevails in all selected azimuths. The phase averaging might have embodied information that could be made evident only by the examination of individual sample signals.

The spectra of the phase-specific signals shown in columns (ii) and (iii) were introduced because, during the course of a simulation, the phase occupying that point may switch between gas and liquid. It is therefore possible that there is not only one type of turbulence that prevails at that point; different forms of turbulence with different energy decay behaviors can be conjectured to prevail during the simulation. Specifically, based on the assertion that turbulence does not cross interfaces, one could conjecture that the less apparent turbulence in the liquid phase makes interpretation of the energy cascade based on a continuous single-fluid velocity signal meaningless.

Comparing the phase-independent spectra and the gas-specific spectra (top row, columns (i) and (ii)), the magnitudes of the energy profiles are virtually the same, since the jetting area is essentially occupied by the gas. The magnitudes of the liquid-specific spectra (top row, column (iii)) are one order smaller. The prevailing $-5/3$ decay law of spectra from all signals in that azimuth confirms that in the region immediately underneath the pipe tip, turbulence is shear-dominated. In the second row, the scatter between energy amplitudes at high wave numbers is significant, and suggests that the intermittency of the phase prevailing in any azimuth is highest for azimuth (b). This is in line with the progressive tendency towards the $-8/3$ power law appearing in the second row. More importantly in the current problem, the $-8/3$ power law – a finding confirmed experimentally by Lance and Bataille (1991) for the liquid-side turbulence – does not seem to be specific to any phase. The $-8/3$ power law slope is seen even more clearly in azimuth (c), and implies a faster energy decay is induced by the presence of fragmented satellite bubbles. The first conclusion to be drawn from the above discussion is that turbulence in the jetting area is dominated by shear, whereas above and to the side of the pipe tip, it is controlled by buoyancy. The second conclusion is that, albeit different in magnitude, continuous phase-independent energy spectra and phase-specific energy spectra provide the same picture of the energy cascade in different portions of the flow. Gas-phase and liquid-phase turbulence are inseparable.

Table 2(a)–(c) shows dissipation rates, and Kolmogorov length and velocity scales, generated from the rms flow field

Table 2
Properties of the turbulence in the flow, in different regions of the domain

	ϵ (kg m^{-1} s^{-3})	ϵ/ρ (m^2 s^{-3})	l_{k} (m)	U_{k} (m s^{-1})
(a)				
Large sub-domain	37.6	9.1×10^{-2}	5.8×10^{-5}	1.7×10^{-2}
Jetting region	1435.4	2.0	2.7×10^{-5}	3.8×10^{-2}
Buoyant rise region	76.7	8.0×10^{-2}	6.0×10^{-5}	1.7×10^{-2}
(b)				
Large sub-domain	1.6	1.6×10^{-3}	1.6×10^{-4}	6.3×10^{-3}
Jetting region	26.7	2.7×10^{-2}	7.9×10^{-5}	1.3×10^{-2}
Buoyant rise region	2.0	2.0×10^{-3}	1.5×10^{-4}	6.7×10^{-3}
(c)				
Large sub-domain	5371.5	13.9	1.7×10^{-5}	6.2×10^{-2}
Jetting region	5331.0	14.0	1.7×10^{-5}	6.2×10^{-2}
Buoyant rise region	5961.8	12.8	1.7×10^{-5}	6.0×10^{-2}

Statistics include the dissipation rate ϵ, the rate normalized by an average void fraction ($\overline{C}$) weighted density ρ, the Kolmogorov length scale l_{k}, and the Kolmogorov velocity scale U_{k}. Different sets of statistics have been obtained, in which point data in the integral computation for ϵ is (a) phase-independent (all data points included), (b) liquid phase-specific (all points of where $\overline{C} < 0.02$) included, and (c) gas phase-specific (all points of where $\overline{C} > 0.50$).

upon which Fig. 6 is based. The dissipation rate, and Kolmogorov length and velocity scales, are determined by

$$\epsilon = \frac{1}{\Omega}\int_{\Omega}(\overline{\mu+\mu_T})\left(\frac{\partial u_i}{\partial x_j}+\frac{\partial u_j}{\partial x_i}\right)^2 \mathrm{d}V, \tag{21}$$

$$l_{\mathrm{k}} = \left(\frac{\overline{\langle v\rangle}^3\overline{\langle\rho\rangle}}{\epsilon}\right)^{1/4}, \tag{22}$$

$$U_{\mathrm{k}} = \left(\frac{\epsilon\overline{\langle v\rangle}}{\overline{\langle\rho\rangle}}\right)^{1/4}, \tag{23}$$

where the overline represents time-averaging (and the operator $\langle\cdots\rangle$ space-averaging in Eqs. (22) and (23)) of bulk-property distributions, and Ω the selected integration domain. Three different sub-domains were used for integration: the entire flow domain minus the regions in the vicinity of the outflow and the outer vertical boundaries, the jetting region underneath the downcomer tip, and the buoyant flow region above it and in a tighter annulus about the pipe. Gas-specific and liquid-specific results were obtained for each region. Local data of $\overline{C} < 0.02$ and $\overline{C} > 0.5$ were used to identify the liquid- and gas-specific dissipation rates, respectively; the upper bound was set because the majority of the domain is essentially liquid. The jetting and buoyant regions feature higher dissipation, and the gas-side turbulence is more pronounced. Given a minimum top-hat filter width of 4.7×10^{-3} m, the Kolmogorov length scales are $O(10^2)$ smaller, thus justifying the need for a higher grid resolution to perform adequate LES of this type of flow. The Smagorinsky kernel for SGS modeling in LES is known to be overly dissipative and to not accommodate backscatter, but in any case the ratio of the filter width to the Kolmogorov scale shows us to be far from a DNS of this bubbling process.

3.8. Interface–turbulence structure correlation

Although Figs. 5 and 7 provide visual evidence of correlation between gas-side turbulence and the interface, they represent only snapshots in time, and are inadequate for any parametric assessment of interface–turbulence coupling. As a first step towards extending the fundamental knowledge of these interaction mechanisms to flows featuring significant topology changes and massive fragmentation and coalescence, we attempt to correlate filtered flow variables that separately quantify the interface and the turbulence.

For that purpose, we first adopt the second invariants of the fluctuating strain rate and vorticity tensors s_{ij} and r_{ij} as potential indicators of turbulence structures, i.e. $|S| = \sqrt{s_{ij}s_{ij}}$ and $|\omega| = \sqrt{r_{ij}r_{ij}}$, where

$$s_{ij} = \frac{1}{2}\left(\frac{\partial u_i'}{\partial x_j}+\frac{\partial u_j'}{\partial x_i}\right) \quad \text{and} \quad r_{ij} = \frac{1}{2}\left(\frac{\partial u_i'}{\partial x_j}-\frac{\partial u_j'}{\partial x_i}\right) \tag{24}$$

denote the fluctuating rates of strain and vorticity. Options for describing the interface deformations include its distance function and its local curvature. Surface curvature computation involves only small storage overhead since it is already determined in the surface force modeling. In contrast, constructing the distance function from 3D VOF data is currently difficult and costly for flows featuring massive stretching, fragmentation and coalescence. Therefore, we consider correlations between strain rate and curvature, and between vorticity and curvature. We actually correlate using the magnitude of the curvature, $|\kappa|$, to best make use of interpolated curvature estimates from CSF-based surface force modeling schemes.

The first correlations considered are space-based measures of interface deformations and turbulence interactions, $\langle \mathrm{Corr}_1(|S|,|\kappa|)\rangle$ and $\langle \mathrm{Corr}_2(|\omega|,|\kappa|)\rangle$, defined by

$$\langle \mathrm{Corr}_1(|S|,|\kappa|)\rangle = \frac{\langle |S|'|\kappa|'\rangle}{\sqrt{\langle |S|'|S|'\rangle}\sqrt{\langle |\kappa|'|\kappa|'\rangle}} \tag{25}$$

($\langle \mathrm{Corr}_2(|\omega|,|\kappa|)\rangle$ is similarly defined). The $\langle\cdots\rangle$ operation represents space-averaging over the support of the interfaces at any instant in time. We then consider the same correlations but over time, denoted by $\overline{\mathrm{Corr}_3(|S|,|\kappa|)}$ and $\overline{\mathrm{Corr}_4(|\omega|,|\kappa|)}$, and defined as

$$\overline{\mathrm{Corr}_3(|S|,|\kappa|)} = \frac{\overline{|S|'|\kappa|'}}{\sqrt{\overline{|S|'|S|'}}\sqrt{\overline{|\kappa|'|\kappa|'}}} \tag{26}$$

($\overline{\mathrm{Corr}_4(|\omega|,|\kappa|)}$ is similarly defined). The overbar represents time-averaging at any point in space. To distinguish, $\langle \mathrm{Corr}_1\rangle$ and $\langle \mathrm{Corr}_2\rangle$; are functions of time, while $\overline{\mathrm{Corr}_3}$ and $\overline{\mathrm{Corr}_4}$ are functions of space.

Fig. 12 shows the spatial correlations of $|S|$ and $|\omega|$ with $|\kappa|$ within the interface support, Corr_1 and Corr_2, at each point in time. The strain and the vorticity correlate with the interface curvature identically. Given that the interface is seen from the gas side like a rigid wall, it is not surprising that bubble movement – be it bubble growth or bubble growth or rise – is accompanied by an internal flow aligning itself with the interface.

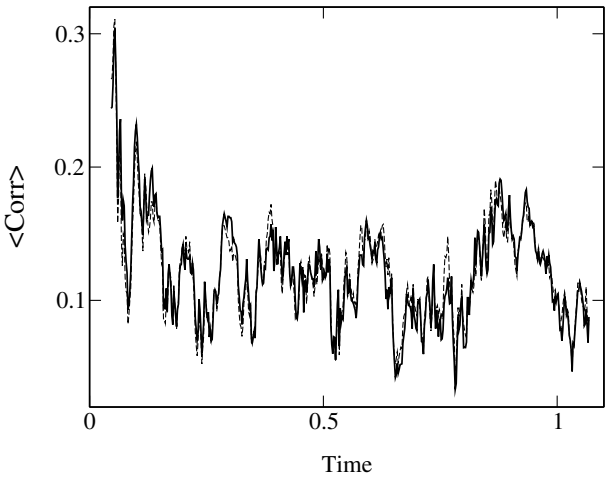

Fig. 12. Time signals of the spatial correlations $\langle \mathrm{Corr}_1(|S|,|\kappa|)\rangle$ (—) and $\langle \mathrm{Corr}_2(|\omega|,|\kappa|)\rangle$ (---). (Time in s.)

Fig. 13 shows the time correlations Corr_3 and Corr_4 at each point within various *xy*-plane slices, as well as in the *xz*- and *yz*-planes through the axis of symmetry in the pipe. The flood contours are used for the correlation distributions themselves, whereas thick line contours show the locations of 0.01, 0.5 and 0.99 time-averaged void-fraction contours; the 0.01 contour is always the outermost void-fraction contour. High correlation regions align with the 0.01 void-fraction contour the best, coinciding with areas where the bubble has expanded out. The results of these two correlations in particular confirm that high-strain, high-vorticity flow regions do indeed coincide with more wrinkled high-curvature surface areas. In general, the vorticity is seen to correlate with curvature slightly better than the strain rate.

Having identified the difference between strain and vorticity magnitudes as bulk distributions and curvature as a property of the interfaces, it is worth noting that the curvature scales inversely with the local interface length scale, and that high-curvature sections of any interface correspond to relative fine wrinkles in the interface.

3.9. Enstrophy/Interface interactions

As an alternative way to separate the contributions of small-scale and large-scale vortical structures on the kinetic energy concentrated at the interface, we introduce the concept of filtered interface-specific enstrophy (ω_{I}^2) and filtered gas-side enstrophy (ω_{G}^2). The first measure is defined as

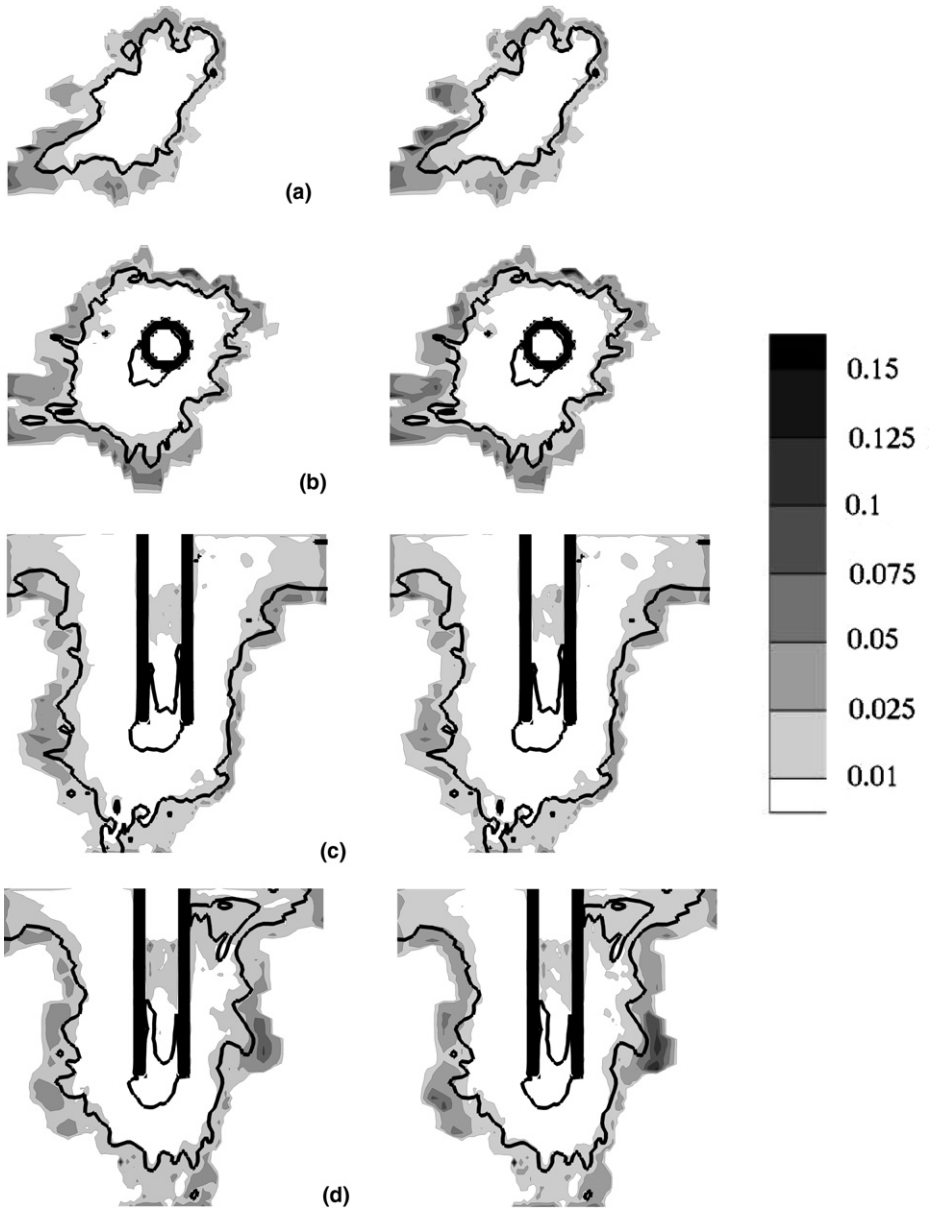

Fig. 13. 2D slices of time-averaged correlations $\overline{\mathrm{Corr}_3(|S|', |\kappa|')}$ (left column) and $\overline{\mathrm{Corr}_4(|\omega|', |\kappa|')}$ (right column): (a) *xy*-plane 1.8*D* below downcomer tip, (b) *xy*-plane at tip level, (c) *xz*-plane through geometric center, (d) *yz*-plane through geometric center.

$$\omega_{\mathrm{I}}^2 = \frac{\sum_{ijk} C_{i,j,k}(1 - C_{i,j,k})(\omega_x^2 + \omega_y^2 + \omega_z^2)}{\sum_{ijk} C_{i,j,k}(1 - C_{i,j,k})}, \tag{27}$$

where the filter $C(1 - C)$ has been introduced to weight contributions such that the function peaks at the interface and reduces to zero in homogeneous regions of the domain. Using this filter helps determine the energy contained by small-scale eddies that directly contact the interface. The gas-side enstrophy is similarly defined by

$$\omega_{\mathrm{G}}^2 = \frac{\sum_{ijk} C_{i,j,k}(\omega_x^2 + \omega_y^2 + \omega_z^2)}{\sum_{ijk} C_{i,j,k}}, \tag{28}$$

where use was made of the color function C to filter out the liquid-side vorticity. The summation is actually performed over a $(4D_{\mathrm{i}})^3$ sub-domain centered around the downcomer tip, in which the probability of the presence of the interface is high. The areas in proximity to the upper boundary are also ignored.

Fig. 14 shows the evolution of ω_{I}^2 and ω_{G}^2 over time. The first feature to note is the temporal alignment of the peaks and troughs in the signals. Gas-side enstrophy ω_{G}^2 is larger than ω_{I}^2 by a factor of about five, suggesting that the majority of the kinetic energy is contained in the large-scale gas-side vortical structures, and less is associated with the surface deformations and fragmentation. The results also suggest that there is a clear out-scatter of vorticity-induced energy, from large-scale motions in the core gas flow, to small scales concentrated at the interface, revealing a strong dependence of the interface topology on the vorticity in the core flow. Having said that though, a non-negligible amount of kinetic energy resides in the small-scale structures associated with the interface wrinkling. FFT of the enstrophy signals yield a few low-frequency peaks – the dominant mode peaks at 6 Hz, while sub-harmonics are visible in the 10–20 Hz range. The similarity of the main mode to the bubbling frequency is notable, but no specific correlation of peaks or troughs with structures in the flow can be clearly established.

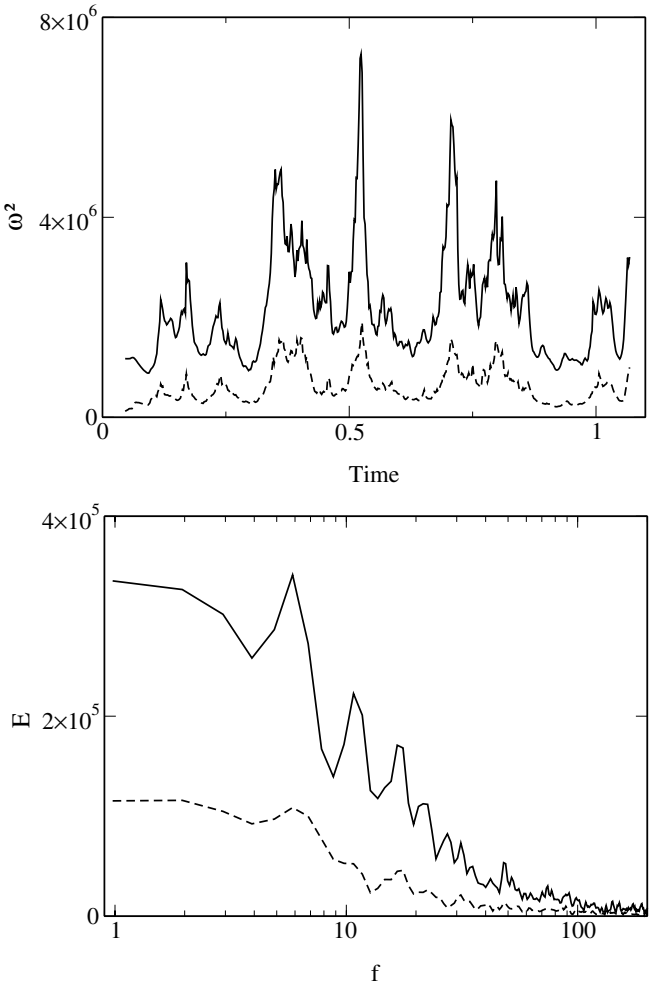

Fig. 14. Time signals and spectra of the square of the enstrophy (ω^2): (- - -) refers to space-averaged enstrophy in the large bubble region isolated to the interface using the $C(1 - C)$ filter, (—) refers to space-averaged gas-side enstrophy (C filter) in the large bubble region. (Time in s, enstrophy in s^{-2}.)

3.10. Interface wrinkling

Turbulence in the vicinity of the interfaces is one potential cause for small-scale wrinkles in chopped-up bubble surfaces. It may also be a mechanism purely driven by interface instability: after the most dominant mode (i.e. the initially spherical-toroidal bubble shape) saturates, it drains energy to its sub-harmonics. To gain insight into the interface wrinkling in this process, we define a bubble-plume (surface) displacement from the axis of symmetry as $r_{C=0.5}(x, y, t)$, which outlines the location of the plume outer surface. The plume outer-surface location is determined by sweeping inwards along rays from the axis

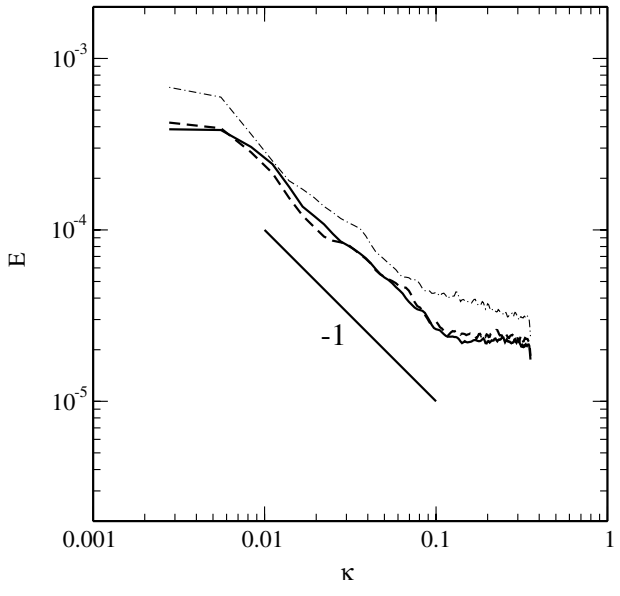

Fig. 15. FFT of bubble-plume displacement $r_{C=0.5}$, where $r_{C=0.5}(\theta)$ are distances along rays emanating from the axis of symmetry to the outermost bubble surface. This distance is an approximation of the outer gas envelope at any point in time. (–·–) Refers to the xy-plane $0.45D_{\mathrm{i}}$ below the downcomer tip, (—) refers to the xy-plane at tip level, and (- - -) refers to the xy-plane $0.9D_{\mathrm{i}}$ above the downcomer tip.

of symmetry at constant intervals $\Delta\theta$, then identifying it as the first location along the ray intersected by the interface. The result represents therefore an outermost extent of the bubble plume, whether it is the surface of the large bubble around the downcomer, or of satellite bubbles. This is the most sensible measure to define, and given that any region of satellite bubbles around the plume is relatively thin compared to the plume, the measure is accurate for the most part. The spectrum of this displacement was extracted for three xy-planes: $0.45D_i$ below the pipe tip, at tip level, and at $0.9D_i$ above pipe level.

The bubble-plume displacements spectra are shown in Fig. 15. In all cases, the spectra of the surface displacements cascade according to a -1 power law, and then give way to leveling out at high wave numbers. The spectra do not exhibit distinct peaks, but rather suggest that interface wrinkling is the ultimate end point of a progressive energy cascading mechanism between surface deformation scales. Energy accumulation at high wave numbers reflects the under-resolution of the interface; the average resolved interfacial scales were already discussed in Section 3.3.

3.11. Sub-filter bubble and drop generation

Fig. 16 shows the cumulative volume function of sub-filter bubbles and drops migrating across the xy-plane at pipe tip level. Sub-filter bubbles and drops are identified to be separate fluid volumes smaller than $(3\delta x)^3$ in size. The results show there to be a steady rate of sub-filter droplet generation during the time-history of the flow, while sub-filter bubble generation is negligible. The number of sub-filter bubbles that are apparent at any point in time crossing the plane ranges from one to four. The results shown in Fig. 16 can be interpreted physically, because small satellite bubble generation is physical (as seen in Fig. 2). However, numerical surface tension is a well-known issue associated with PLIC-VOF schemes, thereby raising the issue of delineating physical and VOF-induced fragmentation. In addition, the idea of incorporating a dispersed phase into VOF-based computations – the sort of two-fluid/single-field hybrid multi-phase flow solver proposed by Cerne et al. (2001) – could be particularly useful for assigning realistic dynamics to the sub-filter bubbles.

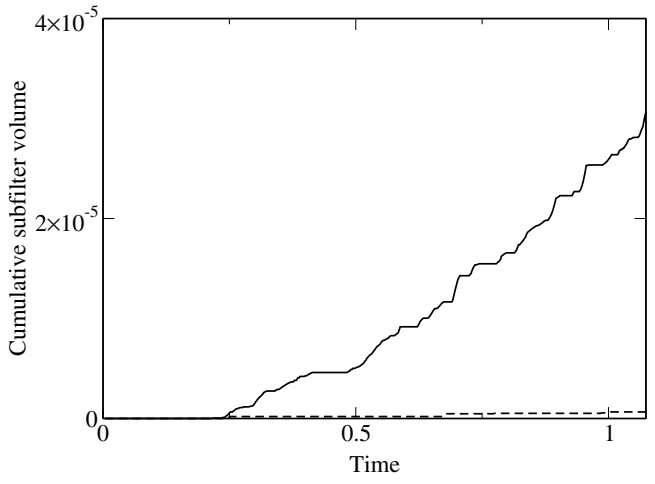

Fig. 16. Cumulative density function of the volume of sub-filter drops (–·–) and bubbles (—) at the downcomer tip level.

4. Conclusions

A novel LES formulation for incompressible multi-fluid flows involving resolvable evolving interfaces has been introduced. The component-weighted filtered single-fluid equations have been presented, and the resulting sub-grid related terms discussed. The method has been applied for a turbulent bubbling process driven by constant volume downward injection of air through a pipe into a water pool. Using a FD/FV-based projection algorithm and robust interface tracking as the core of the method, the LES has delivered turbulence statistics that would be difficult to obtain using other methods. For more modeling-intensive approaches such as the two-fluid approach, the effort required for reliable, scalable modeling is much too daunting.

Interfacial profile comparisons validate the LES as being able to capture the majority of fully 3D effects in bubble growth. The transition from symmetric bubbling featuring smooth surfaces to lop-sided bubbling with chopped-up interfaces is well captured, and so is the generation of fragmentation-induced satellite bubbles. The transition from lop-sided bubble growth back to growth of symmetric bubbles is also captured. Transitions between different modes of bubble growth are not regular in reality, and this is reproduced in the simulations, too. The bubbling frequency is captured correctly to be in the 7–8 Hz range. The qualitative and quantitative macro-scale comparisons of the simulation with experiment validate the simulation as realistically capturing the important transient flow events.

The analysis of the turbulence characteristics of the flow draws the specific conclusions listed below:

- Turbulence is most intense in the gas side; although the liquid-side turbulence is not as obvious, statistical analysis yields energy decay there, too. Turbulence in the shear-dominated jetting region obeys the Kolmogorov K41 slope. Away from the downcomer tip, buoyancy-driven bubble rise coincide with faster energy decay rate, tending occasionally towards the $-8/3$ power law. A less intense turbulence is also generated in the region where vigorous bubble break-up into a swarm of smaller bubbles takes place.
- The decomposition of the interface into azimuthal modes shows an almost linear decay according to a -1 power law, describing a cascade of interfacial radius-of-curvature length scales.
- The cascade of interfacial length scales is accompanied by the out-scattering of vorticity from the large-scale gas-side core flow to the small-scale structures aligning with the interface wrinkling.

Acknowledgments

The authors acknowledge the super-computing resources provided by the Swiss Center for Scientific Computing (CSCS) of Manno. The invaluable contribution of Dr. J.-L. Liow of James Cook University in assisting with computing needs for our work is acknowledged. The authors would like to thank J. Favre of CSCS for his efforts in helping visualize the coherent structures. Finally, the authors would like to thank Prof. B. Geurts, Prof. M. Lance and Prof. G. Yadigaroglu for the invaluable discussions.

References

Brackbill, J.U., Kothe, D.B., Zemach, C., 1992. A continuum method for modeling surface tension. Journal of Computational Physics 100, 335–354.

Bunner, B., Tryggvason, G., 2003. Effect of bubble deformation on the properties of bubbly flows. Journal of Fluid Mechanics 495, 77–118.

Cerne, G., Petelin, S., Tiselj, I., 2001. Coupling of the interface tracking and the two-fluid models for the simulation of incompressible two-phase flow. Journal of Computational Physics 171, 776–804.

Fulgosi, M., Lakehal, D., Banerjee, S., De Angelis, V., 2003. Direct numerical simulation of turbulence in a sheared air–water flow with a deformable interface. Journal of Fluid Mechanics 482, 319–345.

Germano, M., Piomelli, U., Moin, P., Cabot, W.H., 1991. A dynamic subgrid-scale eddy viscosity model. Physics of Fluids 3, 1760–1765.

Hinze, J.O., 1955. Fundamentals of the hydrodynamic mechanism of splitting in dispersion processes. AiChE Journal 1, 289–295.

Hirt, C.W., Nichols, B.D., 1980. Adding limited compressibility to incompressible hydrocodes. Journal of Computational Physics 34, 390–400.

Jeong, J., Hussain, F., 1995. On the identification of a vortex. Journal of Fluid Mechanics 285, 69–94.

Kolev, N.I., 1993. Fragmentation and coalescence dynamics in multiphase flows. Experimental Thermal and Fluid Science 6, 211–251.

Kolmogorov, A.N., 1949. On the disintegration of drops in a turbulent flow. Doklady Akademii Nauk SSSR 66, 825–828.

Lakehal, D., Meier, M., Fulgosi, M., 2002a. Interface tracking for the prediction of interfacial dynamics and heat/mass transfer in multiphase flows. International Journal of Heat and Fluid Flow 23 (3), 242–257.

Lakehal, D., Milelli, M., Smith, B.L., 2002b. Large-eddy simulation of bubbly turbulent shear flows. Journal of Turbulence 3, 1–21.

Lance, M., Bataille, J., 1991. Turbulence in the liquid phase of a uniform bubbly air–water flow. Journal of Fluid Mechanics 222, 95–118.

Liovic, P., Rudman, M., Liow, J.-L., 2002. Numerical modeling of free surface flows in metallurgical vessels. Applied Mathematical Modelling 26, 113–140.

Liovic, P., Lakehal, D., Liow, J.-L., 2004. LES of turbulent bubble formation and breakup by use of interface tracking. In: Geurts, B.J., Friedrich, R., Metais, O. (Eds.), Direct and Large-Eddy Simulation – V, ERCOFTAC Series, vol. 10. Kluwer Academic Publishers, Dordrecht.

Liovic, P., Rudman, M., Liow, J.-L., Lakehal, D., Kothe, D., 2006. A 3D unsplit-advection volume tracking algorithm with planarity-preserving interface reconstruction. Computers and Fluids, available on-line.

Martinez-Bazan, C., Montanes, J.L., Lasheras, J.C., 1999a. On the breakup of an air bubble injected into a fully developed turbulent flow. Part 1. Breakup frequency. Journal of Fluid Mechanics 401, 157–182.

Martinez-Bazan, C., Montanes, J.L., Lasheras, J.C., 1999b. On the breakup of an air bubble injected into a fully developed turbulent flow. Part 2. Size PDF of the resulting daughter bubbles. Journal of Fluid Mechanics 401, 183–207.

Meier, M., 1999. Numerical and Experimental Study of Large Steam-air Bubbles Injected in a Water Pool. PhD dissertation, ETH-Zurich.

Meier, M., Yadigaroglu, G., Andreani, M., 2000. Numerical and experimental study of large steam-air bubbles injected in a water pool. Nuclear Science and Engineering 136, 363–375.

Rider, W.J., Kothe, D.B., 1997. Reconstructing volume tracking. Journal of Computational Physics 141, 112–152.

Risso, F., Fabre, J., 1998. Oscillations and breakup of a bubble immersed in a turbulent field. Journal of Fluid Mechanics 372, 323–355.

van den Akker, H.E.A., 1998. Coherent structures in multiphase flows. Powder Technology 100, 123–136.

Youngs, D.L., 1982. Time-dependent multi-material flow with large fluid distortion. In: Morton, K.W. (Ed.), Numerical Methods for Fluid Dynamics, pp. 273–285.